A Platinum Open Access Journal
for Organic Chemistry

Paper

Free to Authors and Readers

DOAJ Seal

Arkivoc **2024** (3) 202312152

Deciphering CO oxidation on SnO_2 nanosheets: A multinuclear solid-state NMR spectroscopic approach

Xiang Wang,[a,b] Guodong Qi,[a*] Qiang Wang,[a] Jun Xu,[a*] and Feng Deng[a]

[a]National Center for Magnetic Resonance in Wuhan, State Key Laboratory of Magnetic Resonance and Atomic and Molecular Physics, Wuhan Institute of Physics and Mathematics, Innovation Academy for Precision Measurement Science and Technology, Chinese Academy of Sciences, Wuhan, 430071, P. R. China
[b]University of Chinese Academy of Sciences, Beijing, 100049, P. R. China
Email: qgdong@wipm.ac.cn; xujun@wipm.ac.cn

Dedicated to Prof. Graham Hutchings on his 70th birthday

Received mm-dd-yyyy **Accepted Manuscript** mm-dd-yyyy **Published on line** mm-dd-yyyy

Dates to be inserted by editorial office

Abstract

SnO_2 nanosheets exhibit exceptional low-temperature CO oxidation activity, yet the nature of their active sites remains enigmatic. Employing solid-state ^{119}Sn and ^{17}O NMR spectroscopy, we deconstructed the intricate structure of active Sn and oxygen species involved in this process. We identified diverse Sn and O environments, revealing surface Sn_{IV} sites capable of activating O_2 into a critical bidentate η^2–O_2 species responsible for CO conversion into CO_2. In-situ FT-IR spectroscopy studies further revealed the involvement of a carbonate-mediated Mars-van Krevelen mechanism.

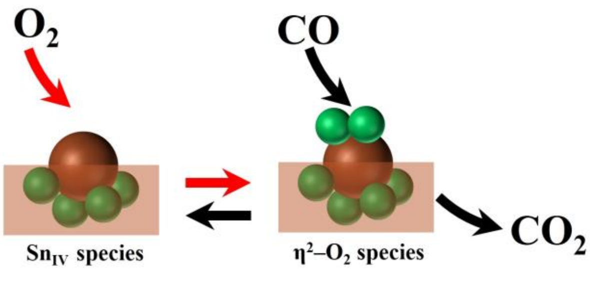

CO oxidation on SnO_2 nanosheets catalyst

Keywords: CO oxidation, SnO_2 nanosheets, active sites, mechanism, NMR spectroscopy

Introduction

As a toxic gas, carbon monoxide (CO) poses risks to human health and the environment. It is commonly found in automobile and factory exhaust gases due to widespread reliance on fossil fuels for energy. It is essential to eliminate CO, especially in confined spaces such as submarines and aerospace stations.[1-3] Among various processes for CO elimination, catalytic oxidation is the most effective approach. Precious metals such as Au,[4-6] Pt,[7-10] and Pd[11, 12] exhibit excellent activity for catalyzing CO oxidation at low temperatures. However, large-scale applications of noble metal catalysts are limited by their scarce reserves and high costs. Therefore, non-precious metal catalysts with abundant reserves and lower costs need to be developed instead.[13] By synthesizing or constructing coordination unsaturated metal active sites,[14-19] such as Fe, Co, Ni, Cu, Zr, Zn, Sn Mn or Mo, non-precious metal catalysts can achieve remarkable catalytic reactivity due to electron transfer between the vacant orbitals of these metal atoms and the reactant molecules. For example, coordination unsaturated Co^{3+} sites on cobalt oxide nanorods can catalyze CO oxidation extremely effectively, even at low temperatures like 196 K.[20] Moreover, monovalent zinc sites confined in zeolite channels can activate molecular oxygen via a single electron transfer mechanism to produce superoxide species, promoting catalytic CO oxidation at room temperature.[21] In addition, coordinatively unsaturated Fe^{2+} confined on Pt nanoparticle surfaces displays high efficiency and selectivity for CO oxidation under hydrogen-rich conditions used in proton-exchange membrane fuel cells.[22]

Tin oxide (SnO_2) with various nanostructures, such as spheres, rods and sheets, has been widely applied in numerous areas including gas sensing,[23] catalysis[24-27] and water photolysis.[28] Regarding catalytic CO oxidation, the reactivity of SnO_2 follows this order: nano-sheets[29,30] > nano-rods[31] > nano-spheres[29]. Therefore, synthesizing SnO_2 nanosheets is a promising approach to improve the CO oxidation activity of SnO_2-based catalysts. However, due to the structural complexity of nano-SnO_2, identifying the structure of active Sn sites and understanding their roles in CO oxidation remains challenging. Hence, the characterization of the active Sn species and elucidating their functions in catalytic reactions, is not only fundamentally important, but also critical for developing efficient nano-SnO_2 catalysts.

Solid-state nuclear magnetic resonance (NMR) spectroscopy has emerged as a powerful technique to provide molecular-level information about active-site structures and their dynamics in heterogeneous catalysis.[32-34] Sn has two NMR spectroscopy-active isotopes, ^{117}Sn and ^{119}Sn, which are both spin 1/2 nuclei with relatively high gyromagnetic ratios (-9.59×10^7 $rad\cdot s^{-1}\cdot T^{-1}$ for ^{117}Sn and -10.03×10^7 $rad\cdot s^{-1}\cdot T^{-1}$ for ^{119}Sn) and natural abundance (7.67 % for ^{117}Sn and 8.58 % for ^{119}Sn). Of note is that ^{119}Sn is commonly used in NMR spectroscopy studies because it has higher sensitivity than ^{117}Sn.[35] Harris and co-workers initiated the solid-state NMR spectroscopic studies of Sn,[36-39] while the first solid state Sn NMR spectrum of SnO_2 was reported by Cossement and co-workers in 1992.[40] In 2016, Chen *et al.* demonstrated that solid-state ^{119}Sn NMR spectroscopy could be employed to monitor the surface structure of nano-sized SnO_2.[41] ^{119}Sn NMR spectroscopic chemical shifts were demonstrated to be able to distinguish Sn atoms in the first, second and bulk layers of nanosheets and their evolution during reactions. Our recent work showed that the proton-detected 2D $^1H\{^{119}Sn\}$ correlation solid-state NMR spectroscopy provides strong evidence for Sn species with Sn-OH structure on zeolites.[42] On the other hand, solid-state ^{17}O NMR spectroscopy is frequently employed to study local structures and oxygen environments,[43,44] although this technique has low sensitivity and complex line shapes due to the intrinsic properties of ^{17}O, e.g. small gyromagnetic ratio, low natural abundance and moderate quadrupole moment. In 2017, Peng and co-workers used solid-state ^{17}O NMR spectroscopy to study the oxygen species on anatase titania nanocrystals with different facets, finding that oxygen ions on the exposed (001) and (101) facets exhibited distinct ^{17}O chemical shifts sensitive to the nanocrystals' surface properties.[45] These solid-state NMR spectroscopy studies offered viable approaches for characterizing metal oxides and related materials. Therefore, combining solid-state ^{119}Sn and ^{17}O NMR spectroscopy could provide a comprehensive characterization of active metal sites by helping to elucidate their roles in the activation of oxygen during catalytic applications.

In this work, we demonstrate a multinuclear solid-state NMR spectroscopic approach to study the mechanism of low temperature CO oxidation on atomically-thin 2D SnO_2 nanosheets synthesized by a solvothermal method.[30] Furthermore, solid-state ^{119}Sn NMR spectroscopy helped identify the coordinatively unsaturated tetrahedral Sn sites serving as the active sites for gas oxygen activation. Lastly, solid-state ^{17}O NMR spectroscopy was applied to determine the active oxygen species generated on these active tin sites. Through the combination of these techniques, the pathway of gas oxygen activation and the mechanism of CO oxidation over this material was thus revealed.

Results and Discussion

Synthesis and catalytic activity of SnO_2 Nanosheets for CO oxidation

The SnO_2 nanosheets were prepared via a previously reported solvothermal synthesis method.[30] Scanning electron microscopy (SEM) and transmission electron microscopy (TEM) images (Figure 1a and 1b) reveal the nanosheet morphology of the obtained SnO_2 catalyst. The X-ray diffraction (XRD) pattern (Figure 1c) confirmed the pure rutile SnO_2 with a tetragonal structure (JCPDS no. 00-041-1445), consistent with previous reports.[30,41] These characterization data provide reliable evidence of the successful synthesis of the atomically thin 2D SnO_2 nanosheets.

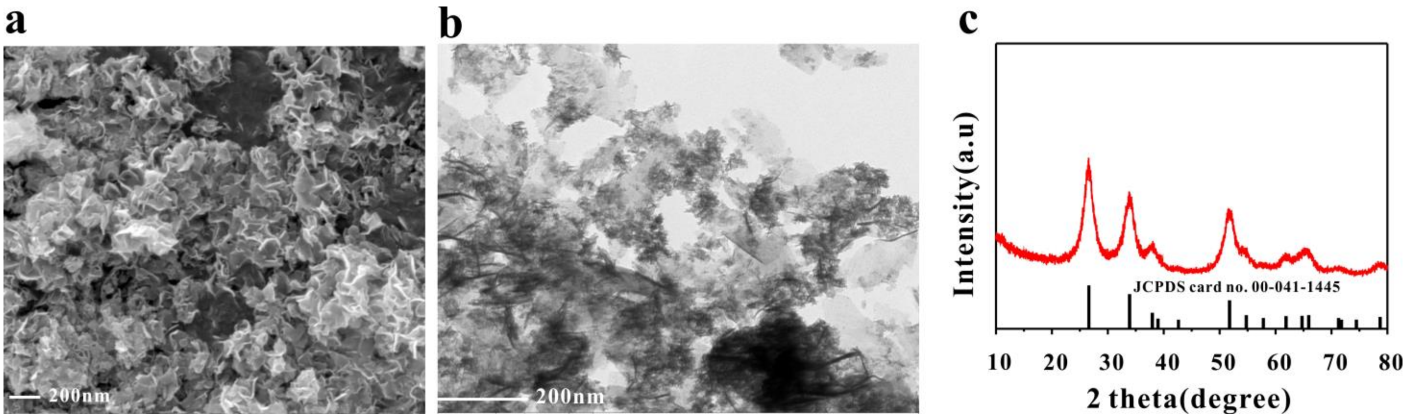

Figure 1. SEM image (a), TEM image (b) and XRD pattern (c) of the synthesized SnO_2 catalyst.

The catalytic performance of the SnO_2 nanosheets for CO oxidation was evaluated next. Figure 2 shows the CO conversion at different reaction temperatures for the SnO_2 nanosheets, before and after reduction with CO. The SnO_2 nanosheets pre-treated with CO demonstrate higher CO oxidation activity compared to the as-synthesized sample (Figure 2a), as evidenced by a much lower T_{50} value (the temperature required to achieve 50% CO conversion) of 128°C for the CO-reduced catalyst versus 283°C for the untreated catalyst. The low-temperature activity of the CO-reduced catalyst is maintained in the first and second reaction cycles, but deactivation occurrs in the third cycle (Figure 2b). These results indicate that CO reduction significantly influences the CO oxidation activity of the SnO_2 nanosheets, suggesting the presence of different active sites or a “changing of availability” for active sites on the catalysts, before and after CO reduction treatment.

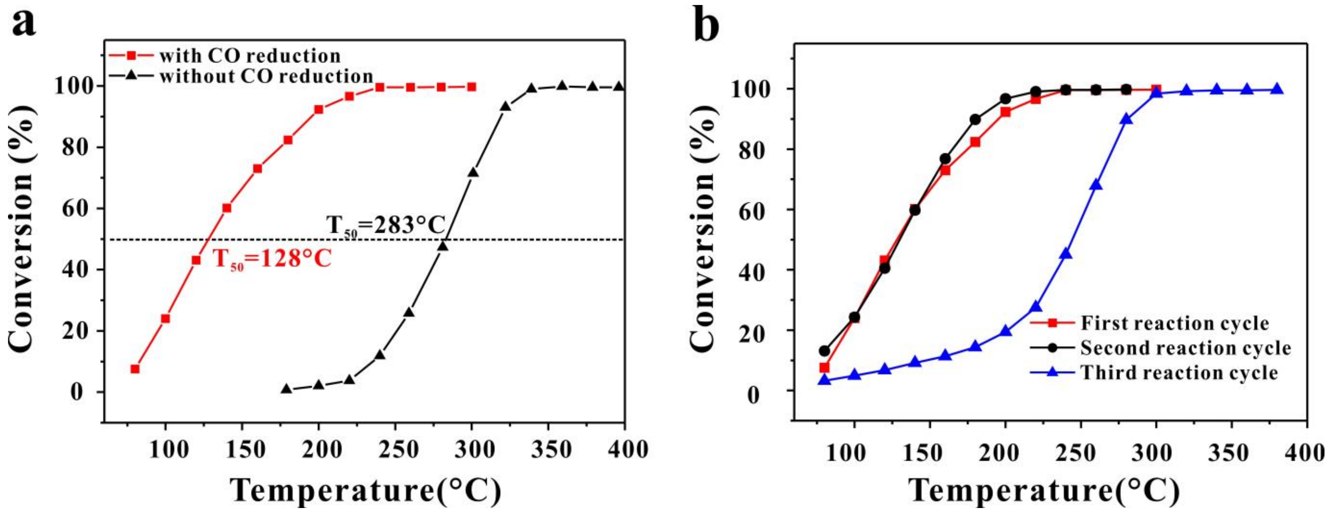

Figure 2. Light-off curves of CO oxidation on the SnO_2 nanosheets, with and without CO reduction (a) and CO conversion on CO-reduced SnO_2 nanosheets at 75 to 400 °C with one to three times reaction cycles (b).

Solid state NMR spectroscopy analysis of active Sn sites

Solid-state ^{119}Sn magic-angle-spinning (MAS) NMR spectroscopy experiments were carried out on the as-synthesized and CO-reduced SnO_2 nanosheets in order to characterize the active Sn sites (Figure 3a and 3b). Four distinct Sn sites were observed with chemical shifts at -568, -586, -604, and -618 ppm in the spectra of both samples. After careful signal simulation, the relative proportions of these signals was obtained as listed in Table 1, entries 1 and 2. Comparing the changes before and after the first CO reduction revealed a significant decrease (from 84.8% to 50.5%) in the strongest signal at -604 ppm, assigned to hexacoordinated Sn (Sn_{VI}) sites on SnO_2 samples.[40,41] Meanwhile, the proportion of Sn sites at -586 ppm increased from 8.5% to 42.9%. Notably, the increase in -586 ppm Sn sites directly corresponded to the decrease in -604 ppm Sn_{VI} sites. The -586 ppm Sn sites likely represents coordination-unsaturated Sn species resulting from CO reduction of Sn_{VI} sites.[46,47] Additionally, the 42.9% proportion of -586 ppm Sn sites on the CO-reduced sample agreed well with the previously reported 40% proportion of surface tetracoordinated Sn (Sn_{IV}) sites on SnO_2 nanosheets.[30] Therefore, we hypothesize that upon exposure to air during preparation, the majority of the surface Sn_{IV} sites on the as-synthesized SnO_2 nanosheets become saturated to Sn_{VI} sites coordinated with oxygen.

To verify this hypothesis, oxygen gas was introduced onto the CO-reduced sample after heating it to 220°C, and the solid-state ^{119}Sn MAS NMR spectrum was recorded (Figure 3c) and analyzed (Table 1, entry 3). As expected, a reduction in Sn_{IV} at -586 ppm, accompanied by an almost equivalent increase in Sn_{VI} at -604 ppm, was observed, suggesting the reversible transformation between surface Sn_{IV} and Sn_{VI} sites. The interconversion between Sn_{IV} and Sn_{VI} was also confirmed by recovering the Sn_{IV} sites when a second CO reduction was applied to the sample after oxidation with O_2 (Figure 3d and Table 1, entry 4). The active role of surface Sn_{IV} sites is demosntrated by their decrease and growth upon O_2 oxidation and CO reduction, respectively. Meanwhile, a loss of active Sn_{IV} sites was observed when comparing the amounts after the first and second CO reductions (Figure 3b and 3d and Table 1, entries 2 and 4), and was found to be consistent with catalyst deactivation in repeat runs (Figure 2b). The proportions of Sn sites at -568 ppm and -618 ppm remained almost unchanged at low levels, regardless of reductive or oxidative treatment. This implied that these Sn sites are probably “spectators” during the CO oxidation process, likely representing sub-surface Sn_{IV} and Sn_{VI} sites whose reduction and oxidation characteristics are inhibited by surface Sn species.

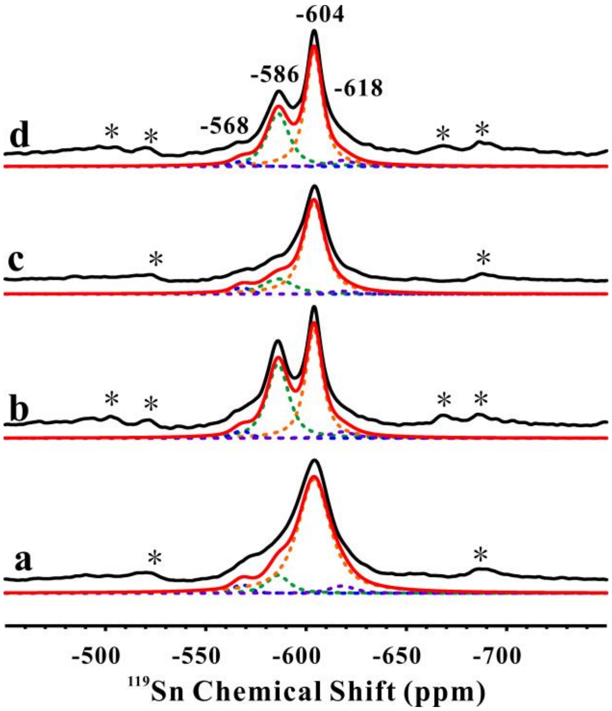

Figure 3. ^{119}Sn MAS NMR spectra of the as-synthesized SnO_2 nanosheets (a), sample (a) with the first CO-reduction at 220°C (b), sample (b) with O_2 oxidation at 220°C (c), and sample (c) with the second CO-reduction at a higher temperature (280°C) (d). The experimental, simulated and deconvolved spectra for each tin sites are represented by solid black lines, solid red lines and colored dash lines, respectively.

Table 1. Quantitative analysis of Sn sites on SnO_2 nanosheets with different treatments based on ^{119}Sn MAS NMR spectral analysis.

SnO_2 nanosheets	The proportion of Sn sites at different chemical shift (%)			
	-568 ppm	-586 ppm	-604 ppm	-618 ppm
As-synthesized	2.5	8.5	84.8	4.2
First CO-reduction	2.5	42.9	50.5	4.1
O_2-oxidized	2.3	17.6	76.3	3.8
Second CO-reduction	2.4	34.3	59.2	4.1

O_2 activation on the coordination-unsaturated Sn sites

Solid-state ^{17}O MAS NMR spectroscopy experiments were employed to explore the interaction between O_2 and the coordination-unsaturated surface Sn_{IV} sites, key to understanding the oxidation mechanism. Experiments were performed at 18.8T with fast 35 kHz MAS for high spectral resolution. Figure 4a shows ^{17}O MAS NMR spectra after introducing $^{17}O_2$ onto SnO_2 nanosheets with different pretreatments. Upon heating $^{17}O_2$-exposed CO-pretreated nanosheets to 220°C, a broad weak singal at 238 ppm, a narrow singal at 137 ppm and overlapping resonances from 0-100 ppm are resolved. 2D ^{1}H-{^{17}O} direct heteronuclear multiple quantum coherence (D-HMQC) NMR spectroscopy was subsequently performed to allow for preliminary signal assignments. As Figure 5 shows, ^{1}H-^{17}O correlations at (5.8, 56), (1.6, 46) and (-0.5, 9) ppm are likely assigned to water-adsorbed, bridging and terminal Sn-OH groups, respectively.[48] Identifying ^{17}O chemcial shifts of Sn-OH groups allowed for the resolution of overlapping resonances (0-100 ppm) by considering isotropic shifts and quadrupole parameters. Besides the three defined OH groups, two signals at 92 and 21 ppm were identified. Site proportions are listed in Table 2, entry 1. To determine the O sites involved in CO oxidation, the $^{17}O_2$-exposed sample (Figure 4a) was reacted with CO at 120 °C near its T_{50} temperature, and examined by ^{17}O MAS NMR spectroscopy (Figure 4b, Table 2, entry 2). The site proportion at 21 ppm noticeably decreased relative to that in Figure 4a, decreasing from 1 to 0.62, while the proportions at other sites only changed slightly. The further $^{17}O_2$ exposure of this CO-reacted sample at 220 °C (Figure 4c, Table 2, entry 3) resulted in the recovery of the 21 ppm site. This strongly suggests that the 21 ppm site serves as the active oxygen species for CO oxidation.

Combining the ^{17}O and ^{119}Sn MAS NMR spectroscopic results, different types of oxygen species on SnO_2 nanosheets are proposed in Figure 6. The proposed process involves bidentate adsorption of gas O_2 on surface Sn_{IV} sites, leaving an η^2–O_2 species and producing Sn_{VI} sites. The formation of η^2–O_2 species requires a two-electrons transformation from the metal to the adsorbed O_2, a process which is commonly found with metal oxides, such as CeO_2.[49] The proportions of 238 and 92 ppm oxygen sites continually increase with $^{17}O_2$ oxidation,suggesting isotope exchange between surface ^{17}O species and 3- or 2-coordinated oxygen in subsurface SnO_2 nanosheet layers. Meanwhile, the 137 ppm oxygen proportion grows after the CO reaction, but reduces after $^{17}O_2$ oxidation (Table 2), probabely due to carbonate formation from the CO adsorption. Additionally, of note was that hydroxyl group proportions varied randomly with redox treatment, excluding them as active sites for CO oxidation.

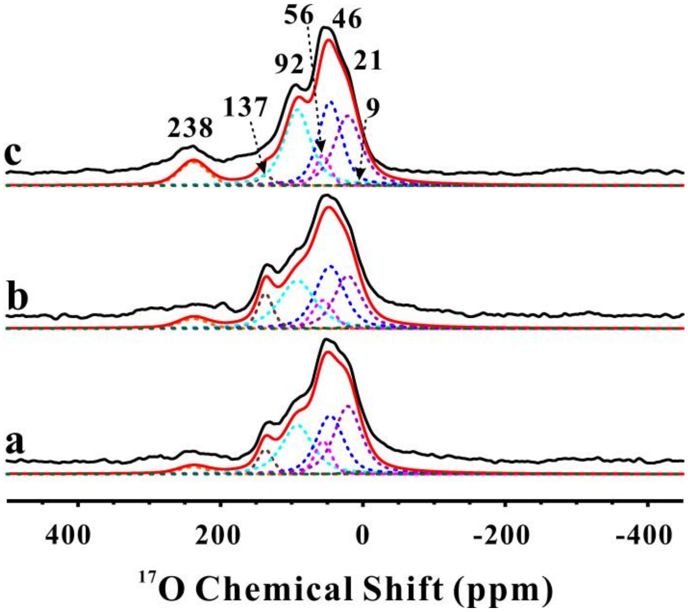

Figure 4. ^{17}O MAS NMR spectra of the firstly CO-reduced SnO_2 nanosheets after being oxidized by $^{17}O_2$ at 220 °C (a), sample (a) reduced by CO at 120°C (b) and sample (b) re-oxidized by $^{17}O_2$ at 220°C (c). The experimental spectra, simulated spectra and deconvolved spectra for each oxygen sites are represented by solid black lines, solid red lines and colored dash lines, respectively.

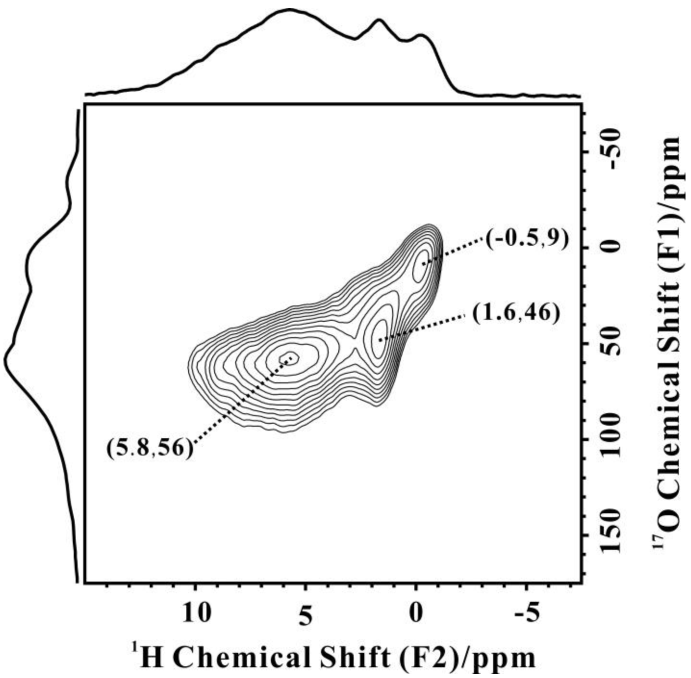

Figure 5. 2D ^{1}H-{^{17}O} D-HMQC NMR spectrum of the firstly CO-reduced SnO_2 nanosheets after being oxidized by $^{17}O_2$ at 220 °C

Table 2. Quantitative analysis of oxygen species on firstly CO-reduced SnO_2 nanosheets after different treatments.

Sample treatment	Oxygen species at different chemical shift[a]				
	238 ppm	137 ppm	92 ppm	The sum of 56, 46 and 9 ppm (hydroxyl groups)	21 ppm
$^{17}O_2$-oxidation	0.10±0.01	0.19±0.01	0.85±0.01	1.13±0.02	1.00±0.01
CO-reduction	0.10±0.01	0.22±0.01	0.79±0.04	1.01±0.03	0.62±0.01
$^{17}O_2$-re-oxidation	0.35±0.04	0.09±0.01	1.22±0.12	1.36±0.13	1.09±0.12

[a] Relative area compared to the reference signal at 21 ppm in Figure 4a. Error ranges were determined through triplicate deconvolution of each spectrum.

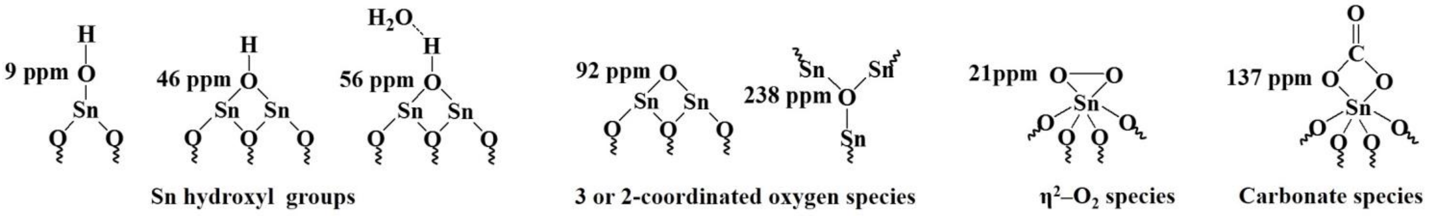

Figure 6. Proposed model of oxygen species produced by $^{17}O_2$ activation on SnO_2 nanosheets. The ^{17}O NMR chemical shift are indicated in the left side of each oxygen sites.

CO oxidation mechanisim catalyzed by coordinationally-unsaturated Sn sites

Several CO oxidation mechanisms have been proposed, including the Langmuir-Hinshelwood and Eley-Rideal pathways which differ in whether O_2 dissociates or reacts directly with CO.[50] These two mechanism are often suggested on noble metal catalysts. The Mars-van Krevelen mechanism is accepted for metal oxide catalysts, where CO reacts with surface oxygen to form CO_2, leaving oxygen vacancies. Molecular O_2 then replenishes the vacancies, recovering surface oxygen in one catalytic cycle.[51]

To gain insight into the CO oxidation mechanism over SnO_2 nanosheets, the reaction process was monitored via *in-situ* diffuse reflectance infrared Fourier transform spectroscopy (DRIFTS-FTIR) (Figure 7a and b). IR band intensities were used to analyze the evolution of CO_2 and carbonate species over reaction time (Figure 7c and d). As shown in Figure 7a and c, after introducing 5 kPa CO to pre-treated SnO_2 nanosheets (via CO reduction then O_2 oxidation), gradual growth of the CO_2 band (2310-2338 cm^{-1}) and carbonate species bands (1600-1300 cm^{-1}) which indicate CO oxidation occurrs with increasing reaction time. Simultaneously, decreasing CO stretching bands (2114-2171 cm^{-1}), which signify CO reactant consumption, are evident. After 20 min of reaction, the *in-situ* IR cell was evacuated and then charged with 5 kPa O_2. Upon further heating for 20 min (Figure 7b and d), a continuous decrease of carbonate species was observed, accompanied by CO_2 formation. These results indicate the intermediate role of carbonate species during CO oxidation. The DRIFTS-FTIR spectroscopy analysis of the evolution of CO_2 and carbonate species showed analogous behavior to the oxygen sites observed at 137 ppm in ^{17}O MAS NMR, thus confirming the assignment of that chemical shift to the carbonate species. We are therefore able to conclude that CO oxidation over SnO_2 nanosheets follows a carbonate-mediated Mars-van Krevelen mechanism, as outlined graphically in Scheme 1. Specifically, coordination-unsaturated Sn_{IV} sites interact with O_2 to form surface bidentate η^2–O_2 species on the surface of SnO_2 nanosheets (Step I). The bidentate η^2–O_2 species exhibit high reactivity with CO, facilitating the transformation to surface carbonate species (Step II). Dissociation of the surface carbonate species then produces CO_2 and a residual oxygen atom (Step III). The residual oxygen atom reacts with an additional CO molecule to yield further CO_2 (Step IV).[52] The catalytic cycle concludes upon regeneration of the coordinatively unsaturated Sn_{IV} sites.

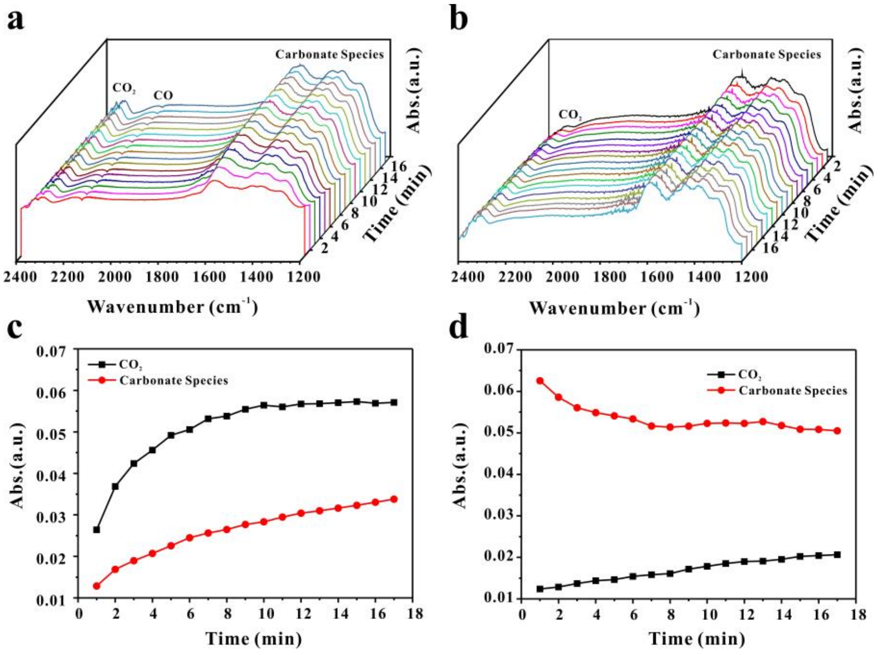

Figure 7. DRIFTS spectra and the evolution of CO_2 and carbonate species over time obtained from a CO (a, c) and O_2 (b, d) reaction cycle on SnO_2 nanosheets at 220 °C.

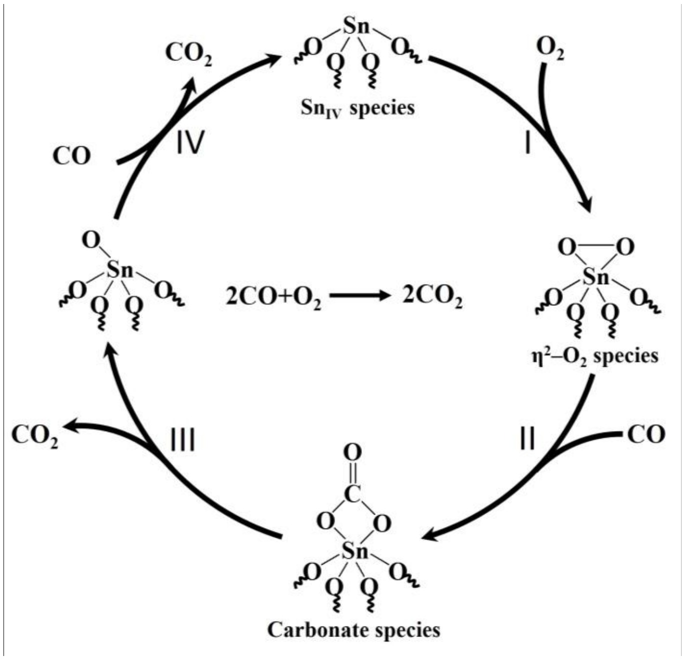

Scheme 1. Proposed catalytic pathway for the reaction of CO oxidation on SnO_2 nanosheets.

Conclusions

By combining solid-state multinuclear NMR spectroscopy and *in-situ* DRIFTS, we have elucidated the detailed structure and dynamic behavior of active Sn and oxygen sites on SnO_2 nanosheets during low-temperature CO oxidation. ^{119}Sn NMR spectroscopy provides compelling evidence for the crucial role of surface Sn$_{IV}$ sites, undergoing reversible Sn$_{IV}$-Sn$_{VI}$ interconversion upon O_2 capture and release, thus facilitating O_2 activation. Furthermore, ^{17}O NMR spectroscopy helped identify a bidentate η^2-O_2 species on the surface Sn sites, generated via a postulated two-electron transfer between Sn$_{IV}$ and O_2, as the key active oxygen species. Integrating these findings with in-situ DRIFTS data, we thus reveal evidence for a carbonate-mediated Mars-van Krevelen mechanism for CO oxidation on SnO_2 nanosheets. Thes results not only deepen our understanding of the catalytic mechanism on nano tin oxides, but also offer valuable insights for the rational design of non-precious-metal oxide catalysts for O_2 activation and related oxidation reactions through strategic manipulation of metal coordination environments.

Experimental Section

Sample preparation

SnO_2 nanosheets were synthesized by direct hydrothermal method in a typical procedure[30], 0.175 g $SnCl_2 \cdot 2H_2O$ was initially added into 70 mL ethylenediamine. After thorough stirring for 60 min, the mixture was transferred into a 100 mL Teflon-lined autoclave, sealed and heated at 180 °C for 48 h. The system was cooled down to room temperature for 12 h, after which the final product was collected by centrifuging the mixture, washing the collected product with distilled water and absolute ethanol (three times), followed by drying under vacuum overnight, to provide material suitable for further characterization and catalytic testing. For CO reduction, 0.04 mmol CO (99.999%) was introduced into the glass tube containing 60 mg pretreated and degassed SnO_2 nanosheets on a vacuum line. The glass tube was sealed with flame and then maintained for 0.5 hours at different temperatures. For O_2 oxidation, the CO in the above procedure was replaced by 0.04 mmol O_2 (99.999%) or $^{17}O_2$ (70%, ^{17}O-abundance). To avoid the exposure of samples to air and water in solid state NMR spectroscopic studies or in-situ DIRFT experiments, material was transferred into a zirconia NMR rotor sealed with a Kel-F end cap or an *in-situ* IR cell in a glove box under dry N_2 atmosphere.

Characterization

The SEM images were performed by using a FEI Nova 400 Nano. TEM images were obtained on a Tecnai G2 20 TWIN transmission electron microscope with an acceleration voltage of 200 kV. XRD patterns were recorded on a Panalytical X' Pert PRO X-ray diffractometer (40 Kv, 40 mA) using CuKα (λ=1.5406 Å) radiation.

Solid-state NMR spectroscopy measurements

^{119}Sn MAS NMR experiments were carried out at 9.4T on a Bruker AVANCE III-400 spectrometer with a 3.2 mm double-resonance probe. The resonance frequencies were 148.82 MHz for ^{119}Sn. Single-pulse excitation ^{119}Sn MAS experiments were performed on the SnO_2 samples by using a π/2 pulse width of 3 µs, a repetition time of 120 s, and a magic angle spinning rate of 12 kHz. The ^{119}Sn chemical shift was referenced to tetracyclohexyltin at -97.4 ppm. Each ^{119}Sn spectrum was accumulated for ca. 12 h. ^{17}O MAS NMR and 2D ^{1}H D-HMQC MAS NMR experiments were carried out at 18.8T on a Bruker AVANCE III -800 spectrometer with 1.9 mm double-resonance probe and the resonance of frequencies were 108.50 MHz and 800.36 MHz for ^{17}O and ^{1}H, respectively. Single pulse MAS experiments were performed on the SnO_2 samples by using a π/2 pulse width of 1.05 µs, a repetition time of 120 s, and a magic angle spinning rate of 35 kHz. The 2D ^{1}H D-HMQC MAS NMR spectra were collected using SR4 recouplings with τ_{re} = 0.15 ms at a spinning speed of 35 kHz, respectively. A total of 128 scans (τ_{re} = 0.15 ms) were collected for the 32 rotor-synchronized t1 increments with recycle delays of 2 s. The ^{17}O chemical shift was referenced to $H_2{}^{17}O$ at 0 ppm and the ^{1}H chemical shift was referenced to adamantane at 1.78 ppm. The ^{17}O MAS NMR spectra were fitted using quadrupolar lineshape with Czsimple model in the DMFIT software. The quadrupolar product parameters were obtained from the ^{17}O MQMAS NMR spectrum of a fully ^{17}O-enriched SnO_2 reference sample.

Catalytic activity measurements

The catalytic properties of CO oxidation for SnO_2 were conducted in a quartz-tube fix-bed reactor using 50 mg catalyst and a mixed gas of 1 vol% CO and 99 vol% dried air at a flow rate of 30 mL/min corresponding to a gas hourly space velocity (GHSV) of 36000 mL h^{-1} g^{-1}. Typically, the catalyst was heated to the desired temperatures at a rate of 2°C min^{-1} and then kept for 30 min until the catalytic reaction reached a steady state. Then, the composition of effluent gas was detected by gas chromatograph (GC 2014, Shimadzu, Japan) equipped with a packed column (TDX-1) and a methane converter in front of a flame ionization detector (FID). Once a cycle was finished, the reactor was cooled to room temperature to start a new cycle. The methane converter is a micro high-temperature furnace (325 °C) with Ni-based catalyst that can fully covert CO and CO_2 into CH_4 for FID detection. The CO conversion was calculated from the change in CO_2 concentration of the inlet and outlet gases.

In-situ DIRFT experiments

The In-situ DIRFT experiments were performed on a Thermo Scientific Nicolet Is 50 instrument. The SnO_2 nanosheets mixed with 90% KBr was packed into the in situ FTIR cell and degased with a pressure below 10^{-3} Pa. CO (5 kPa) was introduced in the cell and heated at 220 °C for 20 min. The cell was degassed and recharged by O_2 (5 kPa) when it was cooled to room temperature. After that the cell was heated at 220 °C for another 20 min. The DRIFT spectra during the heating period were recorded by a mercury-cadmium-telluride (MCT) detector with 16 scans at 4 cm^{-1} resolution. KBr was used for collecting the background spectrum.

Acknowledgements

This work was supported by the National Natural Science Foundation of China (grants 22272185, 22225205, 22320102002 and 22127801), the Magnetic Resonance Technology Alliance of the Chinese Academy of Sciences (2021gzl004), the Strategic Priority Research Program of the Chinese Academy of Sciences (XDB0540000), Hubei International Scientific and Technological Cooperation program (2022EHB021), the Natural Science Foundation of Hubei Province of China (S22H120101), and International Science & Technology Cooperation Base for Sustainable Catalysis and Magnetic Resonance (SH2303)

References

1. Shelef, M.; McCabe, R. W. *Catal. Today*, **2000**, *62*, 35-50.
http://doi.org//10.1016/s0920-5861(00)00407-7
2. Twigg, M. V. *Appl. Catal., B*, **2007**, *70*, 2-15.
http://doi.org//10.1016/j.apcatb.2006.02.029
3. Steele, B. C. H.; Heinzel, A. *Nature*, **2001**, *414*, 345-352.
http://doi.org//10.1038/35104620
4. Haruta, M.; Kobayashi, T.; Sano, H.; Yamada, N. *Chem. Lett.*, **1987**, *16*, 405-408.
https://doi.org/10.1246/cl.1987.405
5. Haruta, M.; Yamada, N.; Kobayashi, T.; Iijima, S. *J. Catal.*, **1989**, *115*, 301-309.
http://doi.org//10.1016/0021-9517(89)90034-1
6. Lou, Y.; Cai, Y.; Hu, W.; Wang, L.; Dai, Q.; Zhan, W.; Guo, Y.; Hu, P.; Cao, X.-M.; Liu, J.; Guo, Y. *ACS. Catal.*, **2020**, *10*, 6094-6101.
http://doi.org//10.1021/acscatal.0c01303
7. Maurer, F.; Jelic, J.; Wang, J.; Gänzler, A.; Dolcet, P.; Wöll, C.; Wang, Y.; Studt, F.; Casapu, M.; Grunwaldt, J. D. *Nat. Catal.*, **2020**, *3*, 824-833.
http://doi.org//10.1038/s41929-020-00508-7
8. Kistler, J. D.; Chotigkrai, N.; Xu, P.; Enderle, B.; Praserthdam, P.; Chen, C. Y.; Browning, N. D.; Gates, B. C. *Angew. Chem. Int. Ed.*, **2014**, *53*, 8904-8907.
http://doi.org//10.1002/ange.201403353
9. Chen, Y.; Feng, Y.; Li, L.; Liu, J.; Pan, X.; Liu, W.; Wei, F.; Cui, Y.; Qiao, B.; Sun, X.; Li, X.; Lin, Lin, J.; Lin, S.; Wang, X.; Zhang, T. *ACS. Catal.*, **2020**, *10*, 8815-8824.
http://doi.org//10.1021/acscatal.0c02253
10. Ding, K.; Gulec, A.; Johnson, A. M.; Schweitzer, N. M.; Stucky, G. D.; Marks, L. D.; Stair, P. C. *Science*, **2015**, *350*, 189-192.
http://doi.org//10.1126/science.aac6368
11. Su, Y. Q.; Filot, I. A. W.; Liu, J. X.; Hensen, E. J. M. *ACS. Catal.*, **2018**, *8*, 75-80.
http://doi.org//10.1021/acscatal.7b03295
12. Gustafson, J.; Balmes, O.; Zhang, C.; Shipilin, M.; Schaefer, A.; Hagman, B.; Merte, L. R.; Martin, N. M.; Carlsson, P. A.; Jankowski, M.; Crumlin, E. J.; Lundgren, E. *ACS. Catal.*, **2018**, *8*, 4438-4445.
http://doi.org//10.1021/acscatal.8b00498
13. Haibach, M. C.; Shekhar, S.; Ahmed, T. S.; Ickes, A. R. *Org. Process Res. Dev.*, **2023**, *27*, 423-447.

http://doi.org//10.1021/acs.oprd.0c00104

14. Gewirth, A. A.; Varnell, J. A.; DiAscro, A. M. *Chem. Rev.*, **2018**, *118*, 2313-2339. http://doi.org//10.1021/acs.chemrev.7b00335
15. Zhu, C. Z.; Li, H.; Fu, S. F.; Du, D.; Lin, Y. H. *Chem. Soc. Rev.*, **2016**, *45*, 517-531. http://doi.org//10.1039/c5cs00670h
16. Li, D. Z.; Liu, H.; Feng, L. G. *Energy Fuels*, **2020**, *34*, 13491-13522. http://doi.org//10.1021/acs.energyfuels.0c03084
17. Singer, R. A.; Monfette, S.; Bernhardson, D. J.; Tcyrulnikov, S.; Hubbell, A. K.; Hansen, E. C. *Org. Process Res. Dev.*, **2021**, *25*, 1802-1815. http://doi.org//10.1021/acs.oprd.0c00104
18. Yao, Z. C.; Tang, T.; Hu, J. S.; Wan, L. J., *Energy Fuels*, **2021**, *35*, 6380-6401. http://doi.org//10.1021/acs.energyfuels.1c00275
19. Liu, H. R.; Shi, S. R.; Wang, Z. H.; Han, Y. H.; Huang, W. *Small*, **2022**, *18*. http://doi.org//10.1002/smll.202103747
20. Xie, X.; Li, Y.; Liu, Z. Q.; Haruta, M.; Shen, W. *Nature*, **2009**, *458*, 746-749. http://doi.org//10.1038/nature07877
21. Qi, G.; Xu, J.; Su, J.; Chen, J.; Wang, X.; Deng, F. *J. Am. Chem. Soc.*, **2013**, *135*, 6762-6765. http://doi.org//10.1021/ja400757c
22. Fu, Q.; Li, W. X.; Yao, Y. X.; Liu, H. Y.; Su, H. Y.; Ma, D.; Gu, X. K.; Chen, L. M.; Wang, Z.; Zhang, H.; Wang, B.; Bao, X. H. *Science*, **2010**, *328*, 1141-1144. http://doi.org//10.1126/science.1188267
23. Kida, T.; Fujiyama, S.; Suematsu, K.; Yuasa, M.; Shimanoe, K. *J. Phys. Chem. C*, **2013**, *117*, 17574-17582. http://doi.org//10.1021/jp4045226
24. Bae, J.; Kim, J.; Jeong, H.; Lee, H. *Catal. Sci. Technol.*, **2018**, *8*, 782-789. http://doi.org//10.1039/c7cy02108a
25. Inomata, Y.; Albrecht, K.; Yamamoto, K. *ACS. Catal.*, **2017**, *8*, 451-456. http://doi.org//10.1021/acscatal.7b02981
26. Kocemba, I.; Rynkowski, J. M. *Catal. Today*, **2011**, *169*, 192-199. http://doi.org//10.1016/j.cattod.2010.09.015
27. Jimenez-Morales, I.; Haidar, F.; Cavaliere, S.; Jones D.; Roziere, J. *ACS. Catal.*, **2020**, *10*, 10399-10411. http://doi.org//10.1021/acscatal.0c02220
28. Chen, X. Q.; Li, L. P.; Zhang, Y. L.; Xu, Y. S.; Li, G. S. *RSC. Adv.*, **2016**, *6*, 83848-83855. http://doi.org//10.1039/c6ra15932j
29. Peng, H.; Peng, Y.; Xu, X.; Fang, X.; Liu, Y.; Cai, J.; Wang, X. *Chinese J. Catal.*, **2015**, *36*, 2004-2010. http://doi.org//10.1016/s1872-2067(15)60926-3
30. Sun, Y.; Lei, F.; Gao, S.; Pan, B.; Zhou, J.; Xie, Y. *Angew. Chem. Int. Ed.*, **2013**, *52*, 10569-10572. http://doi.org//10.1002/anie.201305530
31. Wang, X.; Xiao, L.; Peng, H.; Liu, W.; Xu, X. *J. Mater. Chem. A*, **2014**, *2*, 5616-5619. http://doi.org//10.1039/c3ta15109c
32. Chmelka, B. F. *J. Magn. Reson.*, **2019**, *306*, 91-97. http://doi.org//10.1016/j.jmr.2019.07.051
33. Hunger, M. *Catal. Rev.*, **1997**, *39*, 345-393. http://doi.org//10.1080/01614949708007100
34. Qi, G. D.; Wang, Q.; Xu, J.; Deng, F. *Chem. Soc. Rev.*, **2021**, *50*, 8382-8399. http://doi.org//10.1039/d0cs01130d

35 Harris, R. K.; Becker, E. D.; de Menezes, S. M. C.; Goodfellow, R.; Granger, P. *Magn. Reson. Chem.*, **2002**, *40*, 489-505.
http://doi.org//10.1006/snmr.2002.0063

36. Harris, R. K.; Packer, K. J.; Reams, P. *J. Magn. Reson.*, **1985**, *61*, 564-566.
http://doi.org//10.1016/0022-2364(85)90199-4

37. Harris, R. K.; Packer, K. J.; Reams, P.; Sebald, A. *J. Magn. Reson.*, **1987**, *72*, 385-387.
http://doi.org//10.1016/0022-2364(87)90305-2

38. Harris, R. K.; Mitchell, T. N.; Nesbitt, G. J. *Magn. Reson. Chem.*, **1985**, *23*, 1080-1081.
http://doi.org//10.1002/mrc.1260231211

39. Harris, R. K.; Sebald, A. *Magn. Reson. Chem.*, **1987**, *25*, 1058-1062.
http://doi.org//10.1002/mrc.1260251208

40. Cossement, C.; Darville, J.; Gilles, J. M.; Nagy, J. B.; Fernandez, C.; Amoureux, J. P. *Magn. Reson. Chem.*, **1992**, *30*, 263-270.
http://doi.org//10.1002/mrc.1260300313

41. Chen, J.; Wu, X. P.; Shen, L.; Li, Y.; Wu, D.; Ding, W.; Gong, X. Q.; Lin, M.; Peng, L. *Chem. Phy. Lett.*, **2016**, *643*, 126-130.
http://doi.org//10.1016/j.cplett.2015.11.035

42. Qi, G.; Wang, Q.; Xu, J.; Wu, Q.; Wang, C.; Zhao, X.; Meng, X.; Xiao, F.; Deng, F. *Commun. Chem.*, **2018**, *1*, 22.
http://doi.org//10.1038/s42004-018-0023-1

43. Li, W.; Wang, Q.; Xu, J.; Aussenac, F.; Qi, G.; Zhao, X.; Gao, P.; Wang, C.; Deng, F. *Phys. Chem. Chem. Phys.*, **2018**, *20*, 17218-17225.
http://doi.org//10.1039/c8cp03132k

44. Wang, Q.; Li, W. Z.; Hung, I.; Mentink-Vigier, F.; Wang, X. L.; Qi, G. D.; Wang, X.; Gan, Z. H.; Xu, J.; Deng, F. *Nat. Commun.*, **2020**, *11*, 3620.
http://doi.org//10.1038/s41467-020-17470-4

45. Li, Y.; Wu, X. P.; Jiang N.; Lin, M.; Shen, L.; Sun, H.; Wang, Y.; Wang, M.; Ke, X.; Yu, Z.; Gao, F.; Dong, L.; Guo, X.; Hou, W.; Ding, W.; Gong, X. Q.; Grey, C. P.; Peng, L. *Nat. Commun.*, **2017**, *8*, 581.
http://doi.org//10.1038/s41467-017-00603-7

46. Li, G. X.; Li, S. D.; Han, Z. K.; Zou, C.; Wu, H. L.; Yuan, W. T.; Zhu, B. E.; Gao, Y.; Yang, H. S.; Zhang, Z.; Wang, Y. *Nano. Lett.*, **2021**, *21*, 7309-7316.
http://doi.org//10.1021/acs.nanolett.1c02501

47. Lu, Z.; Ma, D.; Yang, L.; Wang, X.; Xu, G.; Yang, Z. *Phys. Chem. Chem. Phys.*, **2014**, *16*, 12488-12494.
http://doi.org//10.1039/c4cp00540f

48. Wang, J.; Su, Y.; Xu, J.; Ye, C.; Deng, F. *Phys. Chem. Chem. Phys.*, **2006**, *8*, 2378-2384.
http://doi.org//10.1039/b516833c

49. Zhao, Y.; Teng, B. T.; Wen, X. D.; Zhao, Y.; Chen, Q. P.; Zhao, L. H.; Luo, M. F. *J. Phys. Chem. C.*, **2012**, *116*, 15986-15991.
http://doi.org//10.1021/jp3016326

50. Fang, H. C.; Li, Z. H.; Fan, K. N. *Phys. Chem. Chem. Phys.*, **2011**, *13*, 13358-13369.
http://doi.org//10.1039/c1cp21160a

51. Liu, B.; Li, W. P.; Song, W. Y.; Liu, J. *Phys. Chem. Chem. Phys.*, **2018**, *20*, 16045-16059.
http://doi.org//10.1039/c8cp01694a

52. Liu, Y. J.; Lin, L.; Yu, L.; Mu, R. T.; Fu, Q. *J. Phys. Chem. Lett.*, **2023**, *14*, 9780-9786.
http://doi.org//10.1021/acs.jpclett.3c02247